www.czasopisma.pan.pl PAN POLSKA AKADEMIA NAUK www.journals.pan.pl

Arch. Metall. Mater. **67** (2022), 1, 341-348

DOI: https://doi.org/10.24425/amm.2022.137764

JITUO LIU[1], XIANHUI WANG[1*], JIA LIU[2], HANGYU LI[1], YAN LIANG[1], JINGYI REN[1]

INFLUENCE OF COPPER POWDER MORPHOLOGY ON THE MICROSTRUCTURE AND PROPERTIES OF COPPER MATRIX BULK COMPOSITES REINFORCED WITH Ni-DOPED GRAPHENE

To clarify the effect of copper powder morphology on the microstructure and properties of copper matrix bulk composites reinforced with Ni-doped graphene, spherical and dendritic copper powders were selected to fabricate the Ni-doped graphene reinforced copper matrix bulk composites. The Ni-doped graphene were synthesized by hydrothermal reduction method, followed by mixing with copper powders, and then consolidated by spark plasma sintering. It is found that the Ni-doped graphene are well bonded with the dendritic copper powder, whereas Ni-doped graphene are relatively independent on the spherical copper powder. The copper base bulk composite prepared by the dendritic copper powder has better properties than that prepared by spherical copper powder. At 0.5wt.% Ni-doped graphene, the dendritic copper base bulk composite has a good combination of hardness, electrical conductivity and yield strength, which are 81.62 HV, 87.93% IACS and 164 MPa, respectively.

Keywords: Ni-doped graphene; copper base composite; copper powder morphology; mechanical properties

1. Introduction

Since the synergistic effect presents between the matrix material and the reinforcement, the composite has superior properties to its each constituent [1-5]. Due to the excellent electrical and thermal conductivity [6], high Young's modulus [7], mechanical properties [8] and lower density [9], graphene is regarded as the ideal strengthening phase for the composites [10]. However, its large specific surface area and the van der Waals force between the graphene nanosheets give rise to agglomeration, which make it difficult to uniformly disperse on the metal matrix [11,12]. In addition, the poor interface bond between the graphene and the metal matrix hinders the development of graphene metal matrix composites [13-15]. Therefore, it is necessary to search for an appropriate strategy to address these issues.

Thus far, there are extensive investigations on the graphene reinforced Cu matrix composite [16-18]. Generally, the rGO reinforced copper matrix bulk composites have been prepared by various methods, such as the ball milling method, molecular-level mixing method, electrostatic self-assembly method [19-22]. Though the ball milling method [23-25] has high yielding efficiency, it causes the damage of the structural integrity of graphene. The molecular-level mixing method [26,27] can evenly disperse graphene oxide (GO) in the Cu matrix composites, and significantly improve the strength. Gao et al. [28] found that the surface of CTAB coated Cu powders with positive charge adsorbed negatively charge by electrostatic self-assembly method, and the graphene was uniformly dispersed in the copper matrix composites. Graphene decorated with Ag or Ni nanoparticles were fabricated and afterwards successfully introduced as reinforcements into copper matrix. Luo et al. [29] found the Ag-rGO powders were uniformly distributed and securely anchored within the Cu matrix. The Ag nanoparticles could effectively improve the rGO-Cu interface, and promoted the mechanical property of the composites. Nichel nanoparticles anchored on the graphene sheets can effectively prevent the aggregation of grapheme, and improve the interfacial bonding between graphene and copper. It was also discovered that the mechanical behavior of Ni-GNPs/Cu composites is superior than Cu-GNPs/Cu and GNPs/Cu [30-32]. Though much progress has been made from above research, the effect of Cu powder morphology on the microstructure and properties of the graphene reinforced Cu base composite is still obscure.

To disclose the effect of copper powder morphology on the microstructure and properties of graphene reinforced copper

[1] XI'AN UNIVERSITY OF TECHNOLOGY, SCHOOL OF MATERIALS SCIENCE AND ENGINEERING, XI'AN 710048, P.R. CHINA
[2] XI'AN POLYTECHNIC UNIVERSITY, SCHOOL OF MATERIALS SCIENCE AND ENGINEERING, XI'AN 710048, P.R. CHINA

* Corresponding author: xhwang693@xaut.edu.cn

base composites, the rGO doped with nano-sized Ni particles were synthesized by hydrothermal reduction method, followed by respectively mixing Ni-doped graphene (Ni-rGO) and copper powders with dendritic and spherical morphology, and the mixed composite powders were consolidated by spark plasma sintering (SPS). The Ni-rGO composite powder and the sintered materials were examined by X-ray diffractometer, scanning electron microscopy, and the electrical conductivity, hardness and yield strength were tested by conductivity gauge, Vickers hardness tester and universal testing machine, respectively.

2. Experimental

2.1. Synthesis of Ni-doped graphene composite powder

The Ni-rGO were synthesized by hydrothermal reduction method. The GO and nickel nitrate $Ni(NO_3)_2$ were adopted as the precursors, while the hydrazine hydrate is used as the reducing agent. The detailed experimental procedures were as follows. The 50 mg of GO (average thickness 0.8-1.2 nm, size 0.5-5 μm, Nanjing XFNANO Materials Tech Co., Ltd. China) was dispersed into 100 ml of deionized water and sonicated for 2 h to obtain the 0.5 mg/ml GO dispersion. The 0.25 g of nickel nitrate $Ni(NO_3)_2$ was dissolved into the 10 ml absolute ethanol, followed by dropping into the GO dispersion and adjusting the pH value of the mixed solution to 10 by 0.2 mol/L NaOH solution, and then the 10 ml hydrazine hydrate was added dropwise to the mixed solution together with stirring in a water bath at 90°C for 3 h. After cooling to room temperature, it was repeatedly rinsed by centrifugation and subsequently freeze-dried at –50°C to obtain the Ni-rGO composite powders.

2.2. Preparation of Ni-rGO reinforced copper base bulk composites

The Ni-rGO (0 wt.%, 0.5 wt.%, 1 wt.%, 1.5 wt.%) and copper powders with dendritic and spherical morphology were respectively placed in absolute ethanol, followed by ultrasonication for 1 h, and then placed in a 60°C water bath along with stirring till the complete evaporation of the absolute ethanol, and finally the mixed powders of Ni-rGO and copper can be obtained. The composite powders were further mixed in a RM-05 3D rocking mill for 4 h at 30 Hz using the agate milling ball at the ball-to-powder ratio of 4:1. Finally, the composite powders were consolidated in a Labox-330 spark plasma sintering furnace (SPS) at 750°C for 5 min under the pressure of 30 MPa.

2.3. Characterization

X-ray diffraction (XRD) measurements were conducted on a XRD-7000 diffractometer using Cu *Kα* radiation at a wavelength of 1.5406 Å at a scan rate of 8° in the range of 5-90° at the voltage 40 kV and the current of 40 mA. Merlin Compact Zeiss scanning electron microscopy (SEM) and JEM-3010 transmission electron microscopy (TEM) were utilized to examine the powders and composites. Raman spectra were preformed from 100 to 3200 cm^{-1} on an inVia Reflex Confocal Micro-Raman spectrometer using a 532 nm laser. X-ray photoelectron spectroscopy (XPS) analysis was performed on an AXIS ULTRA spectrometer. The relative density, electrical conductivity, hardness and yield strength of the bulk composite were determined by Archimedes method, FQR-7051 eddy conductivity gauge, HV-120 Vickers hardness tester and HT-2402 universal testing machine, respectively.

3. Results and discussion

Fig. 1 shows the XRD patterns of GO and Ni-rGO powders. Apparently, only a single diffraction peak appears at 2θ = 11° for GO powder. However, for the Ni-rGO composite powder, three nickel diffraction peaks present at 44°, 51° and 76°, corresponding to (111), (200) and (220) crystal plane, and no diffraction peak appears at 2θ = 11°. It indicates that nickel ions and GO can be effectively reduced into nickel and graphene after hydrothermal reduction.

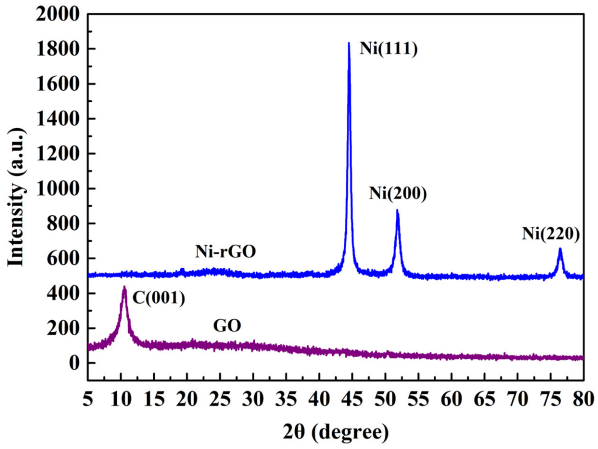

Fig. 1. XRD patterns of GO and Ni-rGO powders

The Ni-rGO composite powders were further examined by SEM and TEM, and the results are shown in Fig. 2. It is evident from Fig. 2(a) and Fig. 2(b) that the graphene sheet is relatively transparent with a very thin thickness and less wrinkles, and the nano-sized Ni particles with the size of approximate 50-200 nm are uniformly dispersed on the graphene sheets. This is because the surface of GO contains a negatively charged oxygen-containing functional groups, the nickel nitrate is dropped into the GO together with synchronous stirring, and the positively charged nickel ions are uniformly adhered on the GO. After hydrothermal reduction, the nickel ions are in situ reduced on the GO surface, followed by nucleation and growth, thus resulting in uniform dispersion of the nano-sized Ni particles on graphene sheets. As determined from a HRTEM micrograph of the Ni-rGO, the

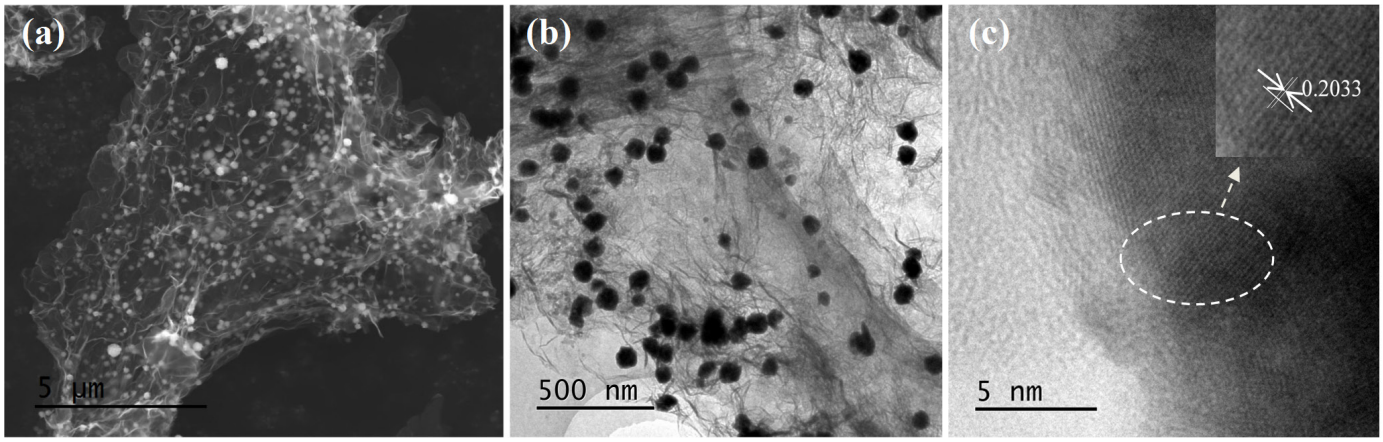

Fig. 2. The images of the Ni-rGO composite powder (a) SEM, (b) TEM, (c) HRTEM

crystal plane spacing is 0.2033 nm, corresponding to the (111) plane of nickel, see Fig. 2(c). Hence, it can be further verified that these particles are nano-sized Ni particles.

Fig. 3 is the Raman spectra of GO and Ni-rGO powders. Apparently, all spectra reveal two prominent peaks, corresponding to the G and D bands, respectively. G band is the characteristic band of carbon materials, which is attributed to the in-plane vibration modes of sp^2 hybridized carbon atoms. D band reflects the change of sp^2-hybridization type of carbon atoms, which is related to the structure defect of graphene [33]. Generally, the defect density of graphene can be evaluated by I_D/I_G value, and the bigger I_D/I_G represents more defects [34]. As seen from Fig. 3, the I_D/I_G value of GO and Ni-rGO are 0.884 and 1.178, respectively. Obviously, the Ni-rGO has a larger I_D/I_G value than GO. It suggests the presence of more isolated new sp^2 domain in Ni-rGO compared to GO and more removal of oxygen groups from GO [35].

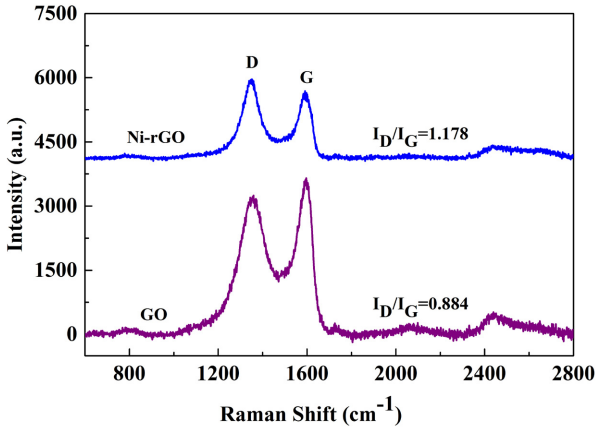

Fig. 3. Raman spectra of GO and Ni-rGO powders

The full XPS spectrum and C 1s XPS spectra of GO and Ni-rGO powders are shown in Fig. 4. As clearly seen from Fig. 4(a) and Fig. 4(c), the C 1s and O 1s peaks present in the full XPS spectrum of GO and Ni-rGO powders. Besides, the Ni 2p peak can be detected in the full XPS spectrum of Ni-rGO composite powder. As seen from Fig. 4(b), four characteristic peaks carbon skeleton (C-C), epoxy group (C-O), carboxyl group (C = O) and carboxylic acid group (O = C-O) indicating that the C elements in GO are mainly existed in these four forms. The peak intensity of C-O, C = O is much lower than that of C-C in Fig. 4(d). The contents of three elements for GO and Ni-rGO powders are given in Table 1. As shown in Table 1, the content of oxygen element in the GO is 28.98 at.%, whereas the content of oxygen element in the Ni-rGO composite powder after hydrothermal reduction is 12.35 at.%, which is reduced by 57.38 % as compared to GO powder. This can further demonstrate that the oxygen-containing functional group of GO powder can be effectively removed by this reduction method. In addition, the content of Ni element in the Ni-rGO composite powder is 3.09 at.%.

TABLE 1

The element contents for the GO and Ni-rGO (at.%)

Element	C 1s	O 1s	Ni 2p
GO	71.02	28.98	—
Ni-rGO	84.56	12.35	3.09

Fig. 5(a) and Fig. 5(b) are the SEM images of the mixture of Ni-rGO and dendritic copper powders at different magnifications, while Fig. 5(c) is the SEM image of the mixture of Ni-rGO and spherical copper powders. As clearly seen from Fig. 5, there are no free nano-sized Ni particles. It suggests that the nano-sized Ni particles are bonded well with rGO. It is worth noting that the Ni-rGO are completely covered on the dendritic copper powder. This is derived from a large contact area of dendritic copper powders and Ni-rGO. However, two-dimensional Ni-rGO have poor matching with the spherical copper powder, which is probably caused by the spherical curvature effect. The similar phenomenon was also reported by Jiang et al. [36]. They studied the difference of adsorption carbon nanotubes capacity between spherical and flake aluminum powders, and found that the flaky geometry can adsorb more carbon nanotubes.

Fig. 6 are the SEM images of different contents of Ni-rGO reinforced copper base composites prepared with the dendritic copper powder, and Fig. 7 are the SEM images of different contents of Ni-rGO reinforced copper base composites pre-

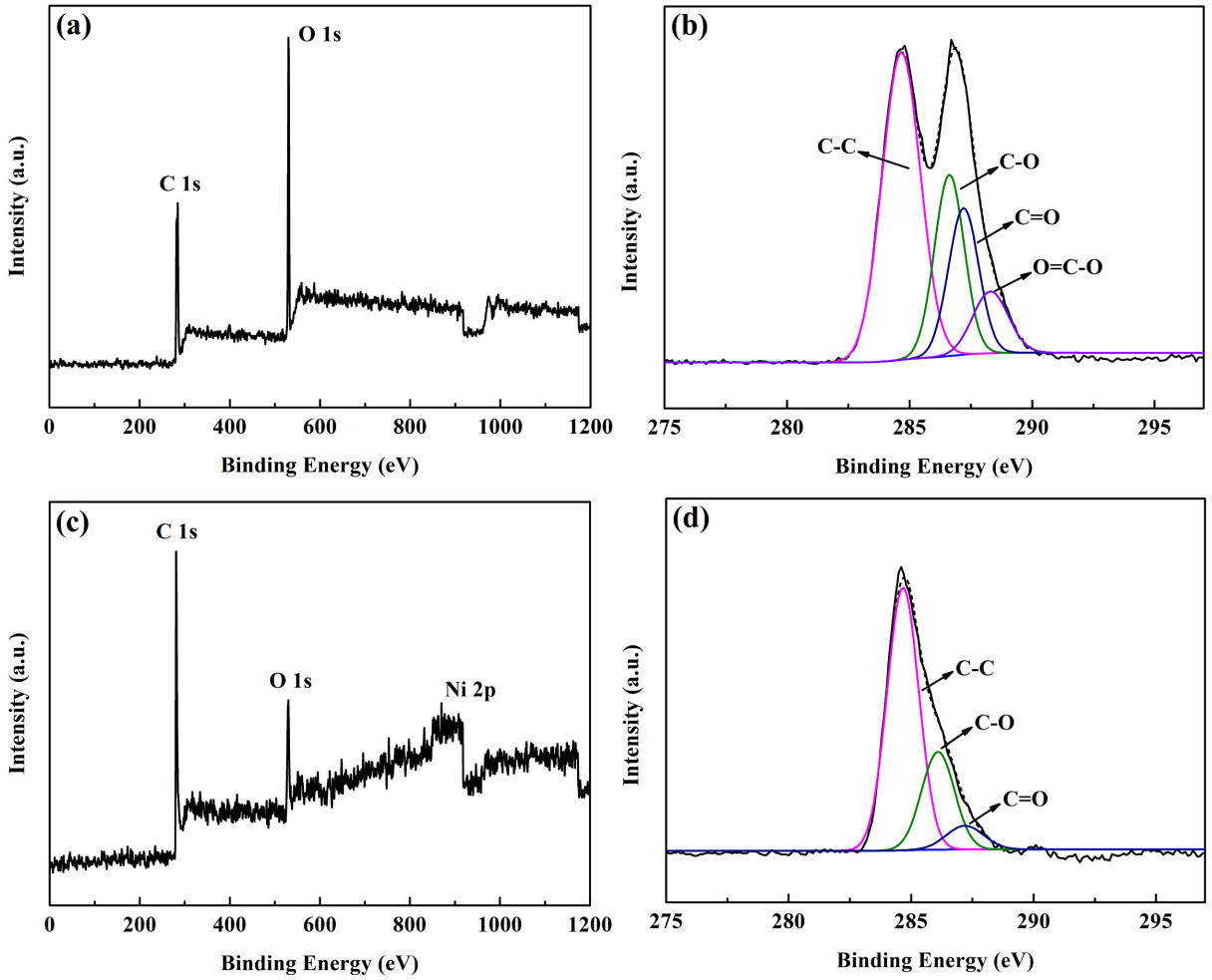

Fig. 4. XPS spectra of GO and Ni-rGO powders (a) XPS full spectrum of GO, (b) C1s XPS spectra of GO, (c) XPS full spectrum of Ni-rGO, (d) C1s XPS spectra of Ni-rGO

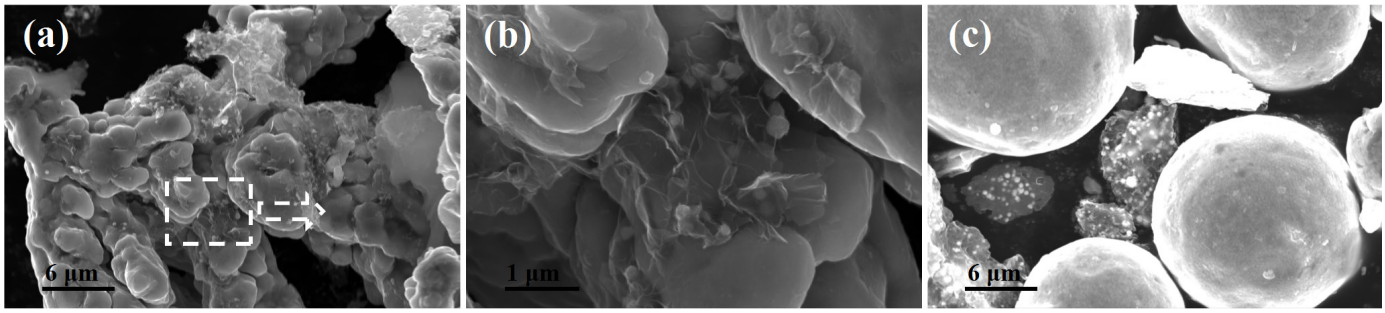

Fig. 5. SEM images of the mixture of Ni-rGO and copper powders with different morphologies (a) dendritic copper powder, (b) the magnified image of the region marked in Fig. 6(a), (c) spherical copper powder

pared with the spherical copper. The black regions are Ni-rGO, while the gray regions are copper matrix. As seen from Fig. 6, at below 1.0 wt.% Ni-rGO, Ni-rGO are uniformly distributed on the dendritic copper matrix. However, a large agglomeration occurs when Ni-rGO is above 1.0 wt.%. As seen from Fig. 7, at 0.5wt.%Ni-rGO, most of Ni-rGO are located at the particle boundary of spherical copper, and a large amount of agglomeration exists in the form of long strips. With increase of Ni-rGO content, serious agglomeration occurs. Based on the above results, it is believed that Ni-rGO have more uniform dispersion in dendritic copper base composite than in spherical copper base composite.

Table 2 are the relative densities of Ni-rGO reinforced copper base composites prepared with dendritic and spherical copper powders. Evidently, the relative density of all sintered materials is above 97%. However, it is also found that the relative density of Ni-rGO/Cu composite decreases slightly with increasing Ni-rGO content. Thus, it is believed that the slightly decreased relative density has a very limited impact on the properties of the composite.

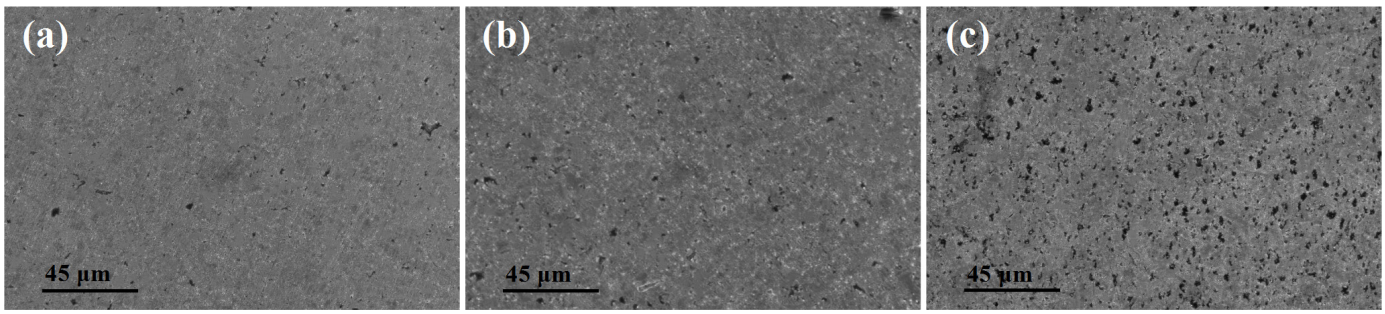

Fig. 6. SEM images of different Ni-rGO reinforced copper base composites prepared with the dendritic copper powder (a) 0.5wt.%Ni-rGO, (b) 1.0wt.%Ni-rGO, (c) 1.5wt.%Ni-rGO

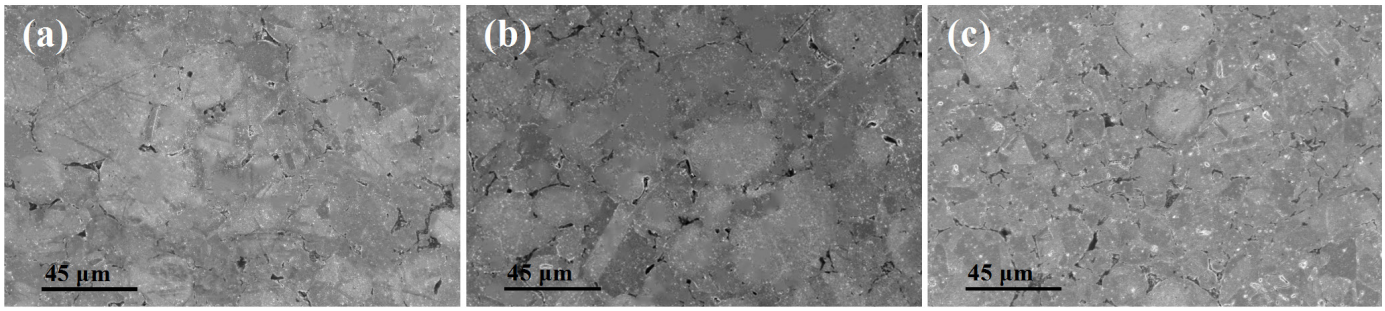

Fig. 7. SEM images of different Ni-rGO reinforced copper base composites prepared with the spherical copper powder (a) 0.5wt.%Ni-rGO, (b) 1.0wt.%Ni-rGO, (c) 1.5wt.%Ni-rGO

TABLE 2

Relative density of Ni-rGO/Cu composites prepared with dendritic and spherical Cu powders

Ni-rGO content (wt.%)	Ni-rGO/dendritic Cu (%)	Ni-rGO/spherical Cu (%)
0	99.44	98.23
0.5	99.32	97.98
1.0	98.75	97.32
1.5	97.93	97.13

Fig. 8(a) shows the variation of the electrical conductivity with Ni-rGO content for the Ni-rGO/Cu bulk composites prepared with dendritic and spherical Cu powders. The electrical conductivity of dendritic Cu matrix composite reinforced by 0 wt.%, 0.5 wt.%, 1 wt.% and 1.5 wt.%Ni-rGO is 89.66%IACS, 87.93%IACS, 70.68%IACS and 54.33%IACS, respectively. Compared with nonreinforced dendritic Cu sinter, the electrical conductivity of dendritic Cu base composites reinforced by 0.5 wt.%, 1 wt.% and 1.5 wt.% Ni-rGO are decreased by 1.9%, 21.2% and 39.4%, respectively. However, for the Ni-rGO reinforced spherical Cu base composite, the electrical conductivity of the composites reinforced by 0 wt.%, 0.5 wt.%, 1 wt.% and 1.5 wt.%Ni-rGO is 84.58 %IACS, 79.52 %IACS, 65.51 %IACS and 48.27 %IACS, respectively. As compared to the pure nonreinforced spherical Cu sinter, the electrical conductivity of 0.5 wt.%, 1 wt.%, 1.5 wt.%Ni-rGO reinforced spherical Cu matrix com-

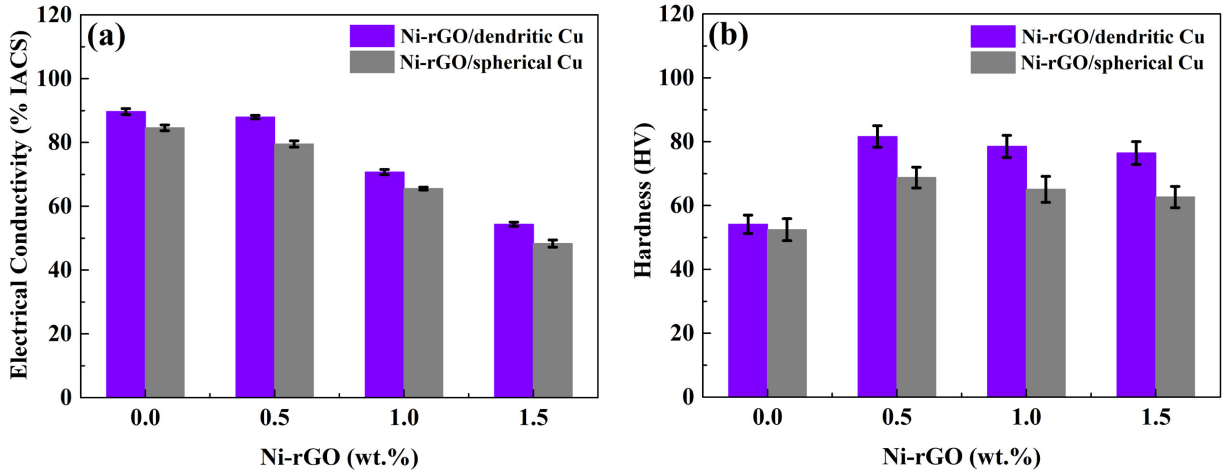

Fig. 8. Variations of the electrical conductivity and hardness with different Ni-rGO reinforced Cu base composites prepared with dendritic and spherical Cu powders (a) electrical conductivity, (b) hardness

posite are decreased by 6.0%, 22.5% and 42.9%, respectively. The composites prepared with dendritic Cu powders have the larger electrical conductivity than that prepared with spherical Cu powders at the same content of Ni-rGO. This can be ascribed to more uniform dispersion of Ni-rGO on dendritic copper.

Fig. 8(b) shows the variation of the hardness with Ni-doped rGO content for the Ni-rGO reinforced Cu base composites prepared with dendritic and spherical Cu powders. For both copper base composites, the hardness increases and then decreases with increasing Ni-rGO content. At 0.5 wt.% Ni-rGO, the maximum hardness values can be reached for both copper base composites reach, which are 81.62 HV and 68.75 HV, respectively. The Ni-rGO hinder the diffusion of copper atoms during the sintering process, which can pin the migration of copper grain boundary and inhibit the growth of copper grains, thus improving the hardness of the composites. However, when the Ni-rGO addition is above 1 wt.%, the decreased hardness can be attributed to the serious aggregation of graphene. From Fig. 8(b), it is also found that the hardness of the composite prepared with dendritic copper powder is always higher than that prepared with spherical copper powder at the same content of Ni-rGO. This is originated from the poor dispersibility of Ni-rGO on the spherical copper matrix composites, and graphene agglomeration hinders the full utilization of graphene properties.

Fig. 9(a) and Fig. 9(b) are the compression stress-strain curves of different Ni-rGO reinforced Cu base composites prepared with dendritic copper and spherical copper powders, and Fig. 9(c) shows their yield strength. Obviously, the yield strength of both copper matrix composites increases and then decreases with increasing Ni-rGO content. The maximum value for both composites can be reached at 0.5 wt.%Ni-rGO, which are 164MPa and 132 MPa, respectively. Compared with spherical copper, the yield strength of 0.5wt.%Ni-rGO reinforced dendritic Cu base composite is increased by 24.2%.

The interfacial bond between graphene and copper can be improved by the nano-sized Ni particles, which is beneficial to transfer the load from matrix to Ni-rGO. According to the modified shear-lag models [32,37,38]. the yield strength of graphene reinforced metal base composite is expressed as:

$$\sigma_c = \sigma_m \left[\left(\frac{V_f (s+4)}{4} + (1 - V_f) \right) \right] \tag{1}$$

$$\sigma_c = \sigma_m (1 + pV_f) \tag{2}$$

$$\sigma_c = \sigma_m \left(1 + \frac{V_f (s-4)}{4} \right) \tag{3}$$

where σ_m and σ_c are the yield strength of pure copper and copper base composites, respectively. V_f is the volume fraction of the graphene, s and p are the shape coefficients of the grapheme, respectively.

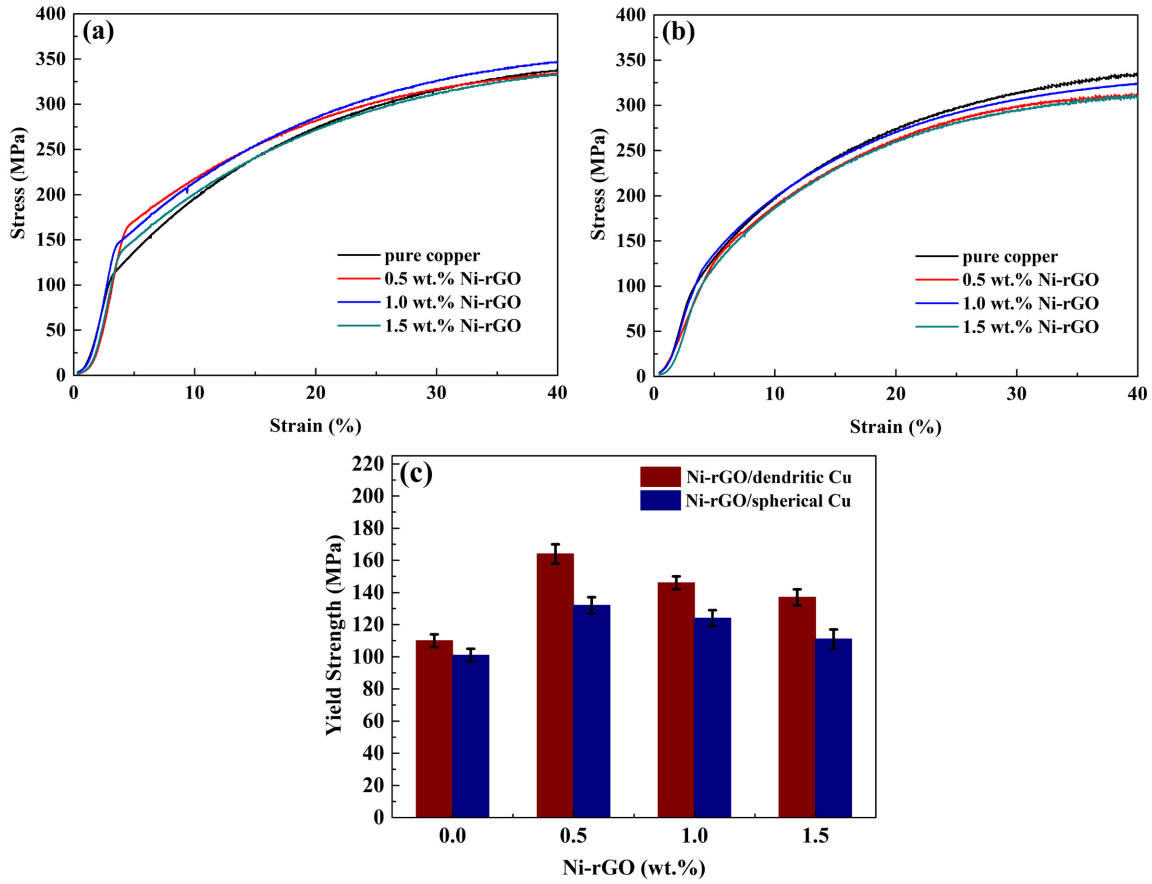

Fig. 9. Compression stress-strain curves and yield strength of different Ni-rGO reinforced Cu base composites prepared with dendritic and spherical Cu powders (a) dendritic Cu base composites, (b) spherical Cu base composites, (c) yield strength

Based on Eq. (1), Eq. (2) and Eq. (3), the following equations could express the increase of yield strength of the graphene reinforced metal base composite:

$$\triangle\sigma_1 = \sigma_m\left[\left(\frac{V_f\left(s+4\right)}{4}-V_f\right)\right] \tag{4}$$

$$\triangle\sigma_2 = \sigma_m p V_f \tag{5}$$

$$\triangle\sigma_3 = \frac{\sigma_m V_f\left(s-4\right)}{4} \tag{6}$$

Therefore, the difference of load transfer strengthening effect between dendritic copper matrix and spherical copper matrix can be expressed as:

$$\triangle_1 = \frac{\triangle\sigma_1^D}{\triangle\sigma_1^S} = \frac{V_f\left(s^D+4\right)+4\left(1-V_f\right)}{V_f\left(s^S+4\right)+4\left(1-V_f\right)} \tag{7}$$

$$\triangle_2 = \frac{\triangle\sigma_2^D}{\triangle\sigma_2^S} = \frac{p^D}{p^S} \tag{8}$$

$$\triangle_3 = \frac{\triangle\sigma_3^D}{\triangle\sigma_3^S} = \frac{s^D-4}{s^S-4} \tag{9}$$

where D and S represent dendritic copper and spherical copper, respectively. p^D and s^D are the shape coefficients of Ni-rGO in dendritic copper matrix. p^S and s^S are the shape coefficients of Ni-rGO in spherical copper matrix.

The modified Shear-lag models is closely related to the aspect ratio of Ni-rGO, so the yield strength of the graphene reinforced Cu base composite depends on the content and aspect ratio of Ni-rGO. If the Ni-rGO have serious aggregation, the corresponding s and p values are higher. It is obvious that the Ni-rGO is agglomerated in the spherical copper matrix, so the s and p of Ni-rGO in the spherical copper matrix are lower than that in the dendrite copper matrix. From Eq. (7), Eq. (8) and Eq. (9), it can be inferred that Δ_1, Δ_2 and Δ_3 are greater than 1. This indicates that the mechanical properties of the graphene reinforced Cu base composite depend on the dispersion of graphene in the Cu matrix. At the same Ni-rGO content, Ni-rGO present the more uniform dispersion in the dendritic copper base composite as compared to the spherical copper base composite, thus possessing higher strength for dendritic copper matrix composite.

4. Conclusions

(1) After hydrothermal reduction, most of oxygen functional groups on the Ni-rGO can be removed, and nickel ions can be effectively reduced to the Ni particles with the size ranging from 50 nm to 200 nm, which are uniformly distributed on the transparent thin rGO sheet.

(2) Ni-rGO have more uniform distribution in the dendritic Cu matrix composite than in the spherical Cu matrix composite, whereas excessive Ni-rGO addition causes the agglomeration in the Cu matrix.

(3) The Ni-rGO reinforced Cu base composite prepared with dendritic copper powders has the superior electrical conductivity, hardness and yield strength as compared to the composite prepared with spherical copper powder.

(4) At 0.5 wt% Ni-doped graphene, the Ni-rGO reinforced Cu base composite prepared with dendritic copper powders has a good combination of the hardness, electrical conductivity and yield strength, which are 81.62 HV, 87.93% IACS and 164 MPa, respectively.

Acknowledgements

This research was supported by the National Natural Science Foundation of China (No. 51971173).

REFERENCES

[1] Y.H. Liang, Z.W. Han, X.J. Li, Z.H. Zhang, L.Q. Ren, Mater. Chem. Phys. **137** (1), 200-206 (2012). DOI: https://doi.org/10.1016/j.matchemphys.2012.09.007

[2] X.L. Wang, Y.P. Wang, Y. Su, Z.G. Qu, Ceram. Int. **45** (12), 14889-14895 (2019). DOI: https://doi.org/10.1016/j.ceramint.2019.04.222

[3] N. Sadeghi, M.R. Akbarpour, H. Aghajani, Mater. Sci. Eng. A **734**, 164-170 (2018). DOI: https://doi.org/10.1016/j.msea.2018.07.101

[4] H.J. Cho, D. Yan, J. Tam, U. Erb, J. Alloy Compd. **791**, 1128-1137 (2019). DOI: https://doi.org/10.1016/j.jallcom.2019.03.347

[5] Q. Zhang, Y. Liu, T. Liao, C.L. Zhang, X.L. Wu, Y.S. Liu, M.S. Qurashi, F. Zheng, Q.S. Song, P. Han, Mater. Chem. Phys. **231**, 188-195 (2019). DOI: https://doi.org/10.1016/j.matchemphys.2018.12.026

[6] W. Zeng, X.M. Tao, S.P. Lin, C. Lee, D.L. Shi, K.H. Lam, B.L Huang, Q.M. Wang, Y. Zhao, Nano Energy **54**, 163-174 (2018). DOI: https://doi.org/10.1016/j.nanoen.2018.10.015

[7] L. Chu, J.J. Shi, R. Braun, Physica E **110**, 115-122 (2019). DOI: https://doi.org/10.1016/j.physe.2019.01.023

[8] F. Lin, Y. Xiang, H.S. Shen, Compos. Part B **111**, 261-269 (2017). DOI: https://doi.org/10.1016/j.compositesb.2016.12.004

[9] J. Wei, C. Luo, H. Li, W. Lv, J.C. Liang, Y.Q. Deng, Z.J. Huang, C. Wang, F.Y. Kang, Q.H. Yang, Carbon **149**, 492-498 (2019). DOI: https://doi.org/10.1016/j.carbon.2019.04.071

[10] C. Salvo, R.V. Mangalaraja, R. Udayabashkar, M. Lopez, C. Aguilar, J. Alloy Compd. **777**, 309-316 (2019). DOI: https://doi.org/10.1016/j.jallcom.2018.10.357

[11] S. Dastjerdi, B. Akgöz, L. Yazdanparast, Compos. Part B **150**, 124-134 (2018). DOI: https://doi.org/10.1016/j.compositesb.2018.05.059

[12] J. Wang, L.N. Guo, W.M. Lin, J. Chen, S. Zhang, S.D. Chen, T.T. Zhen, Y.Y. Zhang, New Carbon Mater. **34** (2), 161-169 (2019). DOI: https://doi.org/10.1016/S1872-5805(19)60009-0

[13] C. Ayyappadas, A. Muthuchamy, A.R. Annamalai, D.K. Agrawal, Adv. Powder Technol. **28** (7), 1760-1768 (2017). DOI: https://doi.org/10.1016/j.apt.2017.04.013

[14] K. Fu, X. Zhang, C.S. Shi, E.Z. Liu, F. He, J.J. Li, N.Q. Zhao, Mater. Sci. Eng. A **715**, 108-116 (2018). DOI: https://doi.org/10.1016/j.msea.2017.12.101

[15] Z. Cao, X.D. Wang, J.L. Li, Y. Wu, H.P. Zhang, J.Q. Guo, S.Q.Wang, J. Alloy Compd. **696**, 498-502 (2017). DOI: https://doi.org/10.1016/j.jallcom.2016.11.302

[16] C.T. Hsieh, Y.F. Chen, C.E. Lee, Y.M. Chiang, K.Y. Hsieh, H.S. Wu, Mater. Chem. Phys. **197**, 105-112 (2017). DOI: https://doi.org/10.1016/j.matchemphys.2017.05.012

[17] S. Perumal, H.M. Lee, I.W. Cheong, J. Colloid Interf. Sci. **497**, 359-367 (2017). DOI: https://doi.org/10.1016/j.jcis.2017.03.027

[18] K.K.H.D. Silva, H.H. Huang, M. Yoshimura, Appl. Surf. Sci. **447**, 338-346 (2018). DOI: https://doi.org/10.1016/j.apsusc.2018.03.243

[19] P.H. Manrique, X.Z. Lei, R.Y. Xu, M.Y. Zhou, I.A. Kinloch, R.J. Young, J. Mater. Sci. **54**, 12236-12289 (2019). DOI: https://doi.org/10.1007/s10853-019-03703-5

[20] H.Y. Yue, L.H. Yao, X. Gao, S.L. Zhang, E.J. Guo, H. Zhang, X.Y. Lin, B. Wang, J. Alloy Compd. **691**, 755-762 (2017). DOI: https://doi.org/10.1016/j.jallcom.2016.08.303

[21] D.D. Zhang, Z.J. Zhan, J. Alloy Compd. **654**, 226-233 (2016). DOI: https://doi.org/10.1016/j.jallcom.2015.09.013

[22] K. Zhang, G.S. Shao, X.H. Chen, W. Li, F.C. Ma, P. Liu, Mater. Lett. **252**, 338-341 (2019). DOI: https://doi.org/10.1016/j.matlet.2019.06.018

[23] W. Ye, Q.Q. Chi, H. Zhou, P. Gao, Int. J. Hydrogen Energy **43** (41), 19164-19173 (2018). DOI: https://doi.org/10.1016/j.ijhydene.2018.08.166

[24] G.S. Shao, P. Liu, K. Zhang, W. Li, X.H. Chen, F.C. Ma, Mater. Sci. Eng. A. **739**, 329-334 (2019). DOI: https://doi.org/10.1016/j.msea.2018.10.067

[25] F. Nazeer, Z. Ma, L.H. Gao, M.A. Khan, A. Malik, F.C. Wang, H.Z. Li, Results Phys. **14**, 102432 (2019). DOI: https://doi.org/10.1016/j.rinp.2019.102432

[26] J. Hwang, T. Yoon, S.H. Jin, J. Lee, T. Kim, S.H. Hong, S. Jeon, Adv. Mater. **25** (46), 6724-6729 (2013). DOI: https://doi.org/10.1002/adma.201302495

[27] L.D. Wang, Y. Cui, B. Li, S. Yang, R.Y. Li, Z. Liu, R. Vajtai, W.D. Fei, RSC Adv. **5** (63), 51193-51200 (2015). DOI: https://doi.org/10.1039/C5RA04782J

[28] X. Gao, H.Y. Yue, E.J. Guo, H. Zhang, X.Y. Lin, L.H. Yao, B. Wang, Powder Technol. **301**, 601-607 (2016). DOI: https://doi.org/10.1016/j.powtec.2016.06.045

[29] H.B. Luo, Y.W. Sui, J.Q. Qi, Q.K. Meng, F.X. Wei, Y.Z. He, J. Alloy Compd. **729**, 293-302 (2017). DOI: https://doi.org/10.1016/j.jallcom.2017.09.102

[30] D.D. Zhang, Z.J. Zhan, J. Alloy Compd. **658**, 663-671 (2016). DOI: https://doi.org/10.1016/j.jallcom.2015.10.252

[31] Y.J. Mai, F.X. Chen, W.Q. Lian, L.Y. Zhang, C.S. Liu, X.H. Jie, J. Alloy Compd. **756**, 1-7 (2018). DOI: https://doi.org/10.1016/j.jallcom.2018.05.019

[32] Y.X. Tang, X.M. Yang, R.R. Wang, M.X. Li, Mater. Sci. Eng. A. **599**, 247-254 (2014). DOI: https://doi.org/10.1016/j.msea.2014.01.061

[33] X.S. Li, Y.B. Zhao, W. Wu, J.F. Chen, G.W. Chu, H.K. Zou, J. Ind. Eng. Chem. **20** (4), 2043-2049 (2014). DOI: https://doi.org/10.1016/j.jiec.2013.09.029

[34] J. Chen, Y. Zhang, M. Zhang, B.W. Yao, Y.R. Li, L. Huang, C. Li, G.Q. Shi, Chem. Sci. **7** (3), 1874-1881 (2016). DOI: https://doi.org/10.1039/C5SC03828F

[35] S. Thakur, N. Karak, Carbon **50** (14), 5331-5339 (2012). DOI: https://doi.org/10.1016/j.carbon.2012.07.023

[36] L. Jiang, G.L. Fan, Z.Q. Li, X.Z. Kai, D. Zhang, Z.X. Chen, S. Humphries, G. Heness, W.Y. Yeung, Carbon **49** (6), 1965-1971 (2011). DOI: https://doi.org/10.1016/j.carbon.2011.01.021

[37] S.J. Yan, S.L. Dai, X.Y. Zhang, C. Yang, Q.H. Hong, J.Z. Chen, Z.M. Lin, Mater. Sci. Eng. A. **612**, 440-444 (2014). DOI: https://doi.org/10.1016/j.msea.2014.06.077

[38] H.P. Zhang, C. Xu, W.L. Xiao, K. Ameyama, C.L. Ma, Mater. Sci. Eng. A. **658**, 8-15 (2016). DOI: https://doi.org/10.1016/j.msea.2016.01.076